



Nanostructured F doped IrO_2 electro-catalyst powders for PEM based water electrolysis

Karan Sandeep Kadakia ^a, Prashanth H. Jampani ^a, Oleg I. Velikokhatnyi ^{b, c},
Moni Kanchan Datta ^{b, c}, Sung Kyoo Park ^b, Dae Ho Hong ^b, Sung Jae Chung ^d,
Prashant N. Kumta ^{a, b, c, d, e, *}

^a Department of Chemical and Petroleum Engineering, Swanson School of Engineering, University of Pittsburgh, PA 15261, USA

^b Department of Bioengineering, Swanson School of Engineering, University of Pittsburgh, PA 15261, USA

^c Center for Complex Engineered Multifunctional Materials, University of Pittsburgh, PA 15261, USA

^d Department of Mechanical Engineering and Materials Science, Swanson School of Engineering, University of Pittsburgh, PA 15261, USA

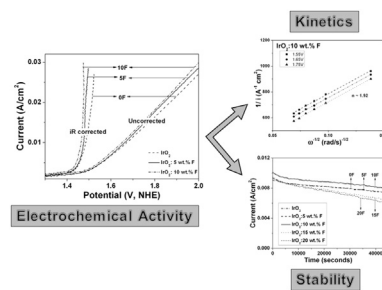
^e Department of Oral Biology, School of Dental Medicine, University of Pittsburgh, PA 15217, USA



HIGHLIGHTS

- Nanostructured $\text{IrO}_2:\text{F}$ electro-catalysts have been wet chemically synthesized.
- $\text{IrO}_2:10$ wt.% F exhibits superior electrochemical activity than pure IrO_2 .
- Stability of the $\text{IrO}_2:\text{F}$ nanomaterials is comparable to pure IrO_2 .
- High surface area F doped IrO_2 are promising OER anode electro-catalysts.
- Both half-cell and full cell test data show the superior response of $\text{IrO}_2:10$ wt.% F.

GRAPHICAL ABSTRACT



ARTICLE INFO

Article history:

Received 9 March 2014

Received in revised form

7 July 2014

Accepted 8 July 2014

Available online 16 July 2014

Keywords:

PEM water electrolysis

F doped IrO_2

Nanostructured

High surface area

Electro-catalyst

ABSTRACT

Fluorine doped iridium oxide ($\text{IrO}_2:\text{F}$) powders with varying F content ranging from 0 to 20 wt.% has been synthesized by using a modification of the Adams fusion method. The precursors (IrCl_4 and NH_4F) are mixed with NaNO_3 and heated to elevated temperatures to form high surface area nanomaterials as electro-catalysts for PEM based water electrolysis. The catalysts were then coated on a porous Ti substrate and have been studied for the oxygen evolution reaction in PEM based water electrolysis. The $\text{IrO}_2:\text{F}$ with an optimum composition of $\text{IrO}_2:10$ wt.% F shows remarkably superior electrochemical activity and chemical stability compared to pure IrO_2 . The results have also been supported via kinetic studies by conducting rotating disk electrode (RDE) experiments. The RDE studies confirm that the electro-catalysts follow the two electron transfer reaction for electrolysis with calculated activation energy of $\sim 25 \text{ kJ mol}^{-1}$. Single full cell tests conducted also validate the superior electrochemical activity of the 10 wt.% F doped IrO_2 .

© 2014 Elsevier B.V. All rights reserved.

1. Introduction

Hydrogen has been universally claimed as a potential next generation energy carrier with the tremendous ability to provide clean, reliable and affordable energy to meet the ever-increasing

* Corresponding author. Department of Bioengineering, 815C Benedum Hall, 3700 O'Hara Street, Pittsburgh, PA 15261, USA. Tel.: +1 412 648 0223; fax: +1 412 624 3699.

E-mail address: pkumta@pitt.edu (P.N. Kumta).

global energy demands [1]. A major barrier limiting the progress towards realization of the hydrogen economy is production, storage and distribution of low cost, carbon-free and ultra-high purity (UHP) hydrogen to meet our sustainability goals. High quality hydrogen can be benignly produced by electrochemical conversion of water using electricity *i.e.*, water electrolysis. The high cost of electricity to date has thus far always hindered the production of electro-catalytic hydrogen [2–4]. Electricity induced splitting of water despite the cost nevertheless, offers no pollutants or the creation of toxic by-products if the electricity is generated *via* renewable energy sources such as the use of photovoltaic cells, wind turbines, geothermal and hydropower. If all of the limitations, and the barriers discussed above are overcome, we can envision the hydrogen fuel and hydrogen technology to provide a very plausible and ecologically sustainable option for energy production if the efficiency of water electrolysis can be significantly improved with considerable reduction in costs [5–9].

The current technologies using proton exchange membrane (PEM) or acid based water electrolysis are very cost intensive. This impedes us from achieving the targeted hydrogen production cost (~\$ 3.0/gasoline gallon equivalent (gge)). High capital costs are encountered due to the expensive noble metal catalysts currently employed combined with the inferior efficiencies and labor intensive fabrication of PEM based electrolyzers [4,5,10–14]. PEM based electrolysis however, display several advantages over alkaline and neutral pH based water electrolysis processes including, but not limited to, high proton conductivity, low gas crossover, compact stack design, higher current densities, high pressure operation and the desired chemical and electrochemical tolerance [6,10,15]. At the anode, the over-potential and the ohmic resistance however results in poor electrochemical activity accounting for the sluggish catalytic performance. The durability of the electro-catalysts is also a major issue under the harsh acidic PEM conditions, thereby making the search for efficient and stable catalysts a high priority and a major imperative need if the much desired progress in this area is to be achieved.

Rutile type noble metal oxides, such as IrO_2 and RuO_2 are well known and accepted as gold standard anode catalysts for the oxygen evolution reaction (OER) in PEM based water electrolysis. Decrease in the noble metal oxide ($\text{IrO}_2/\text{RuO}_2$) loading with improved catalytic activity would enable much reduction in capital costs of PEM electrolyzer cells. It has been reported previously by many researchers [16–27] that addition of cheaper metal oxides or diluents (*viz.*, SnO_2 , Ta_2O_5 , TiO_2 , Nb_2O_5) to the parent noble metal oxide resulting in a binary or ternary metal oxide mixture could reduce the overall noble metal oxide content. However, with the addition of the cheaper diluents results in a reduction in the active surface area and electronic conductivity of the mixed oxides [17,18,24,28–30].

We have shown in various publications [16,27,31–34] the viability and efficacy of fluorine as a dopant combined with the use of solid solutions of binary and ternary systems as efficient electro-catalysts for water electrolysis. Specifically, F doped IrO_2 as a thin film electro-catalyst for OER in PEM based electrolysis has been previously reported by us [31]. Fluorine doping resulted in ~20% increase in electrochemical catalytic activity. The stability of the catalysts was also comparable to pure IrO_2 . We also performed first principle theoretical calculations using the *ab-initio* approach [32] that concluded that electrolytic water splitting utilizing F doped IrO_2 could contribute to significantly increasing the catalytic activity. This initial study formed the basis for motivating the development of F doped IrO_2 catalysts in the form of nanomaterials and also conduct detailed studies on the same.

In the present study, research is carried out to synthesize nanostructured F doped IrO_2 electro-catalysts in order to improve

the catalytic activity and the corrosion stability of the doped oxide compared to pure noble metal oxide electro-catalyst. In this article, F doped IrO_2 , denoted as $\text{IrO}_2:x$ wt.% F or $\text{IrO}_2:\text{F}$, with $x = 0, 5, 10, 15$ and 20 have been synthesized using a modification of the Adams fusion approach [35] and tested as an OER electro-catalyst. The catalyst ink is then coated on a porous Ti foil and tested as an anode electro-catalyst for PEM water electrolysis. In order to achieve a better understanding of the fundamental electrochemical reactions or electro-catalytic activity, detailed characterization analyses comprising X-ray diffraction (XRD), transmission electron microscopy (TEM), electrochemical impedance spectroscopy (EIS), Tafel analysis, rotating disk electrode (RDE) experiments, and chronoamperometry (CA) studies have been performed and reported on the synthesized $\text{IrO}_2:\text{F}$ nanostructured powder electro-catalysts.

2. Experimental details

2.1. Electro-catalyst preparation

Iridium tetrachloride [IrCl_4 , 99.5%, Alfa Aesar], and ammonium fluoride [NH_4F , 98%, Alfa Aesar] were used as the precursor sources for Ir and F, respectively. $\text{IrO}_2:\text{F}$ was synthesized using a modification of the Adams fusion method, first reported by Adams et al. [35], and used by other researchers as well [36,37]. The precursors were taken in stoichiometric amounts and completely dissolved in D.I. water generated by the Milli-Q system [18.2 $\text{M}\Omega \text{ cm}$ deionized water; Milli-Q Academic, Millipore]. The solution containing the dissolved precursors were mixed with excess sodium nitrate [NaNO_3 , 99%, Alfa Aesar] also dissolved in D.I. water to generate the corresponding nitrate precursors in the dissolved state. The resulting solution mixture was stirred vigorously for 2 h to generate a homogeneous solution following which the water is then carefully evaporated at 60 °C. The mixture is then introduced into a furnace wherein it is heated to 500 °C at a ramp rate of 50 K min⁻¹, and then held at 500 °C for 1 h to form the F doped IrO_2 . The salt mixture is then washed multiple times with D.I. water in order to remove all the undesired excess chloride salts. The resulting homogeneous fluoride containing oxide powder is then dried in an oven at 60 °C for 24 h to form the $\text{IrO}_2:x$ wt.% F electro-catalyst, where x ranges from 0 to 20.

2.2. Physical and chemical characterization

The synthesized electro-catalysts were analyzed by X-ray diffraction using state-of-the-art detector [XRD, Philips XPERT PRO system with $\text{CuK}\alpha$ radiation]. Typical scans were recorded in the 2θ range of 20°–80°. The operating voltage and current were kept constant at 45 kV and 40 mA, respectively. Specific surface area of the catalysts was measured using the Brunauer–Emmett–Teller (BET) technique. The powders were first vacuum degassed and then tested using a Micromeritics ASAP 2020 that employs nitrogen adsorption and desorption for surface area analysis. Correspondingly, multipoint BET surface areas are reported for the synthesized nanostructured powder. The microstructure and particle size of the catalysts was investigated using high resolution transmission electron microscopy (HRTEM). JEOL 4000EX operating at 400 kV was employed for conducting the TEM analysis to evaluate the particle size and nanocrystalline nature. High resolution transmission electron microscopy (HRTEM) analysis was conducted on the samples using JEOL JEM-2100F to further investigate the morphology.

2.3. Electrochemical testing and kinetics studies

Electrochemical characterization was conducted on the samples using a five port jacketed reaction cell [Ace Glass Inc.] assembled

with the three electrode test system as described in our previous publications [16,17,27,31,34]. The electrochemical experiments were performed using a VersaSTAT 3 [Princeton Applied Research]. A solution of 1 N sulfuric acid was used as the electrolyte/fuel which is kept at a constant temperature of 40 °C using a Fisher Scientific 3006S Isotemp refrigerated circulator. The working electrodes were prepared by uniformly spreading the catalyst ink on a titanium foil [50% porosity, Accumet Materials Co.] on an area of 1 cm². The catalyst ink consisted of 85 wt.% catalyst and 15 wt.% Nafion 117 solution [5 wt.% solution in lower aliphatic alcohols, Sigma–Aldrich]. The total loading on the Ti foil for all the electro-catalyst compositions was ~0.3 mg cm⁻². The reference electrode was an XR 200 mercury/mercurous sulfate electrode [Hg/Hg₂SO₄, Radiometer Analytical] with a potential of ~+0.65 V with respect to the standard hydrogen electrode (SHE/NHE). Platinum foil [Alfa Aesar, 0.25 mm thick, 99.95%] was used as the counter electrode. All the polarization tests were conducted employing a scan rate of 1 mV s⁻¹.

Electrochemical impedance spectroscopy (EIS) measurements have been used to determine the solution resistance, and the polarization resistance of the electro-catalyst using a suitable circuit model such as $R_s(R_{ct}Q_{dl})$, where R_s is the solution/ohmic resistance, R_{ct} is the charge transfer resistance/polarization resistance, and Q_{dl} includes both the double layer capacitance and pseudocapacitance [38,39]. EIS has been performed in the frequency range of 100 mHz–100 kHz using the VersaSTAT 3 [Princeton Applied Research]. Impedance data has been modeled using the ZView software from Scribner Associates. R_s is used for ohmic loss (iR) correction, whereas R_{ct} enables the understanding of the electrochemical activity of the electro-catalyst. The Tafel plot after iR correction is given by Equation (1):

$$\eta = b \log i + a \quad (1)$$

Here, ' η ' is the overpotential, ' b ' is the Tafel slope, ' i ' is the current density and ' a ' determines the exchange current density. The corresponding Tafel slope (b), is used to determine the reaction kinetics [38,40,41].

Rotating disk electrode (RDE) experiments have been carried out in order to obtain information about the kinetics and detailed mechanisms of the electrochemical reaction. The studies provide confirmation of the number of electrons transferred in the OER process, and also calculate the apparent activation energy of the reaction. The RDE tests were performed in a three electrode system, using the same reference electrode and counter electrode as described before. A titanium disk insert [5 mm OD, 4 mm thick, mirror polish; Pine Research Instrumentation] was used for the working electrode. The catalyst ink was deposited on the Ti disk and dried in an ethanol saturated environment overnight. The disk was then heated to 130 °C for 2 h. A multiple small potential step measurement has been used for all the RDE measurements, first used by Chu et al. [42]. Potential steps of 5 mV are given starting from the open circuit potential and current is recorded at every potential for 16 s. The last value of the current is then taken into consideration for accurate analysis i.e., there is a decay time of 15 s in order to ensure that the electrode double layer charging current and the adsorption current is negligible [42]. The RDE experiments have been executed by using varying speeds from 500 rpm to 2000 rpm. The Koutecky–Levich plot represented by Equation (2); involving the kinetic current (i_k) and Levich current (i_L) as shown in Equations (3) and (4) respectively, is widely used for RDE studies conducted in this work [42–44]:

$$i^{-1} = i_k^{-1} + i_L^{-1} \quad (2)$$

$$i_k = knAFC \quad (3)$$

$$i_L = 0.62nFAD^{2/3}\omega^{1/2}v^{-1/6}C \quad (4)$$

where, ' i ' is the current [Ampere (A)], ' k ' is the kinetic rate constant of the reaction (cm s⁻¹), ' n ' is the electron transfer number, ' A ' is the electrode area (0.19625 cm²), ' F ' is the Faraday constant [96485 (A-s) mol⁻¹], ' C ' is the concentration of reactive species (1.3×10^{-6} mol cm⁻³), ' D ' is the diffusion coefficient (1.7×10^{-5} cm² s⁻¹), ' ω ' is the rotation rate (radians s⁻¹), and ' v ' is the viscosity (0.01 cm² s⁻¹) [44–48]. The slope of the Koutecky–Levich plot i.e., i^{-1} vs. $\omega^{-1/2}$ helps determine the number of electrons (n) transferred in the reaction and the intercept gives the kinetic rate constant (k) of the reaction.

The influence of temperature on the OER process has been studied in order to calculate the apparent activation energy (E_a). In the RDE setup, a high rotation speed of 1500 rpm was used and the multiple small potential step measurement technique as mentioned before was carried out in the temperature window of 25 °C–70 °C. The Arrhenius relation as expressed in Equation (5) is given by:

$$i = k_0 \exp(-E_a/RT) \quad (5)$$

where, ' k_0 ' is the pre-exponential factor, ' E_a ' is the apparent activation energy (J mol⁻¹), ' R ' is the universal gas constant (8.314 J mol⁻¹ K⁻¹), and ' T ' is the temperature (K). A plot of $\ln i$ vs. T^{-1} i.e., the Arrhenius plot would help in determination of the apparent energy of activation [49–52].

In order to study the long term structural stability of the electro-catalysts, chronoamperometry (CA) i.e., current signal as a function of time has been conducted. Testing of the electrodes has been performed for 12 h using 1 N H₂SO₄ at 40 °C at a constant voltage of ~1.65 V (vs. NHE) without iR correction. Elemental analysis of the electrolyte (H₂SO₄), collected after CA testing, was performed by inductively coupled plasma optical emission spectroscopy (ICP-OES, iCAP 6500 duo Thermo Fisher) in order to determine the amount of iridium leached out into the solution from the electrode.

2.4. Single full cell test analysis

The catalyst ink for the anode and cathode consisted of 85 wt.% catalyst and 15 wt.% Nafion 117 solution (5 wt.% solution in lower aliphatic alcohols, Sigma–Aldrich). In order to test the performance of the catalyst under electrolyzer conditions, a single cell test was performed at Proton OnSite. For the single cell testing, a membrane electrode assembly was fabricated by using a Nafion 115 membrane sandwiched between the two gas diffusion electrodes coated with the catalyst ink. The cathode catalyst used for the single cell test was platinum black (Sigma Aldrich) supported on a Teflon treated carbon paper (Electrochem Inc.). The anode material used for the test comprised the best electro-catalyst composition synthesized i.e., IrO₂:10 wt.% F which was also compared with pure IrO₂ (undoped). The backing layer used on the anode side was titanium felt (60% porosity, Electrochem Inc.). The Nafion 115 membrane was pretreated first with a 3 wt.% hydrogen peroxide solution taken to its boiling point in order to oxidize any organic impurities. Subsequently, it was boiled in D.I. water followed by immersion in a boiling 1 N sulfuric acid solution to eliminate any metallic impurities. Finally, it is treated multiple times in D.I. water to remove any traces of remnant acid. This membrane is then stored in D.I. water to avoid dehydration. The membrane electrode assembly (MEA) was then fabricated by placing the two Nafion impregnated electrodes (anode and cathode) on both sides of the pretreated Nafion

membrane. This assembly was then hot-pressed in a 25 T hydraulic lamination hot press with dual temperature controller (MTI Corporation) at a temperature of 125 °C. The pressure applied was approximately 40 atm for ~30 s to ensure good contact between the electrodes and the membrane. This 5 layer MEA is then used for conducting the single full cell electrolyzer tests.

The 5 layer MEA prepared was then sandwiched between two Teflon gaskets of 5 mils thickness. The area of the electrodes and the hole in the gaskets was a square area of 5 cm². This assembly is then placed in Proton's test cell and the tests were conducted at the Proton OnSite facility (Wallingford, CT). All the samples were heat soaked by flowing 65 °C water throughout the cell for 1 h prior to testing. The polarization curve was taken at 50 °C by ramping up the current, stepping in 1 min intervals of 100 mA cm⁻². The polarization curve was then run back down at 1 min intervals. The polarization curves were then run back up and down at 1 min intervals until the forward and reverse scans basically overlaid each other.

3. Results and discussion

3.1. Structural characterization

X-ray diffraction, specific surface area measurements and transmission electron microscopy characterization was conducted in order to study the phase purity and crystalline nature of the electro-catalysts synthesized. The XRD patterns of the IrO₂:F powders after heat treatment to 500 °C are shown in Fig. 1. The XRD patterns show a rutile type tetragonal structure similar to pure IrO₂ for all the synthesized electro-catalysts. No additional peak (Example, iridium fluoride) is observed which indicates the formation of a complete single phase solid solution of F incorporated into IrO₂ without inducing any undesired phase separation as observed previously [31]. This might arise due to the fact that the ionic radius of O²⁻ (125 pm) is comparable to that of F¹⁻ (120 pm) [53]. The relative broad peaks seen in the XRD patterns (Fig. 1) are clearly indicative of the nanocrystalline nature of the synthesized catalysts. The effective crystallite size of IrO₂:F, calculated using the Scherrer formula from the integral breadth of the Lorentzian contribution determined from the peak profile analysis using single line approximation method after eliminating the instrument line broadening and lattice strain contribution [54] is ~3–4 nm for different F compositions which is similar to that of pure undoped IrO₂ (~4 nm).

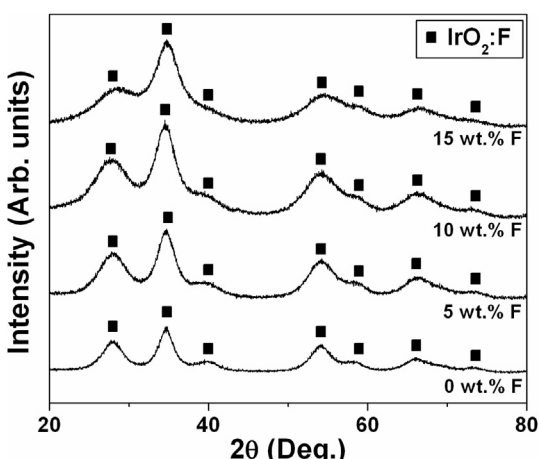


Fig. 1. The XRD pattern of the nanostructured IrO₂:F of different compositions.

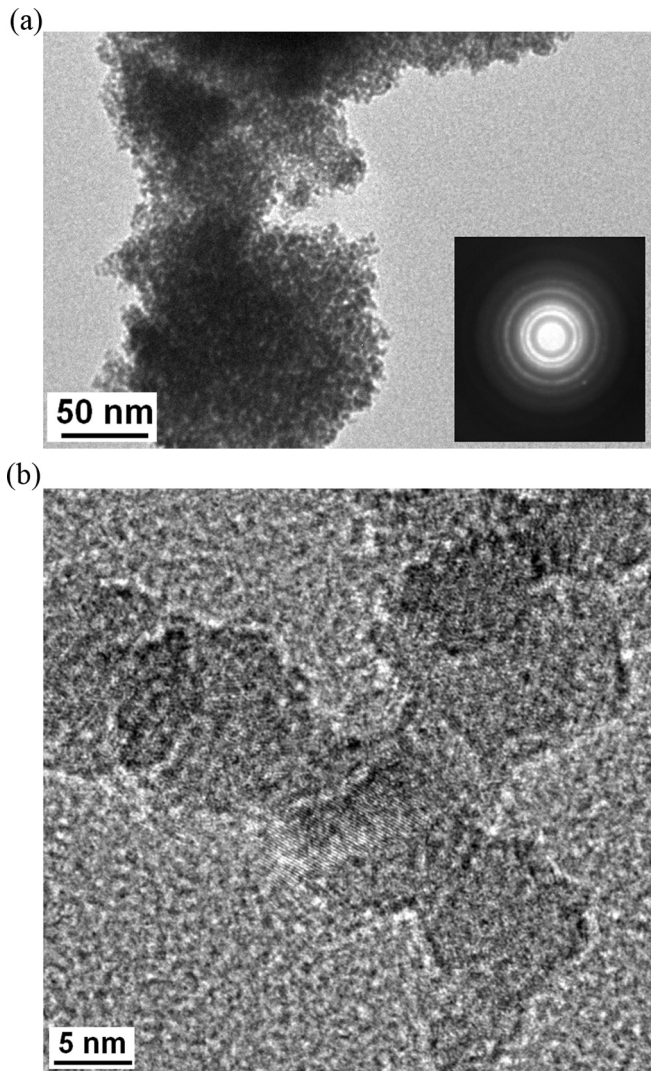


Fig. 2. The bright field TEM image (a), and the HRTEM image (b) of IrO₂:10 wt.% F particles; confirming the nanostructured nature of the electro-catalysts.

The specific surface area (SSA) of IrO₂:F measured by the BET technique ranged from 100 to 200 m² g⁻¹ for varying F compositions. Pure IrO₂ exhibited an SSA of ~191 m² g⁻¹ while IrO₂:x wt.% F displayed an SSA of ~184 m² g⁻¹, 157 m² g⁻¹, 129 m² g⁻¹ and 100 m² g⁻¹ for x = 5, 10, 15 and 20 wt.% of F, respectively. These SSA values are much higher than that corresponding to commercial IrO₂ [Alfa Aesar] which is ~20 m² g⁻¹. The decrease in the SSA of IrO₂:F with increasing F incorporation might be because of the heat released due to the exothermic phenomenon of NH₄F burning, occurring during the synthesis of the catalyst powders. This heat released could cause agglomeration of IrO₂:F nanoparticles causing a decrease in the SSA [55]. Another possible mechanism could also be due to rapid diffusion of F¹⁻ into the lattice causing grain growth resulting in reduction in the surface area. A decrease in the specific surface area with incorporation of F for other materials and catalyst systems has also been reported by other researchers too [55–58]. The bright field TEM image shown in Fig. 2a, of a representative electro-catalyst composition of IrO₂:10 wt.% F confirms the nanometer size (~5–10 nm) state of the particles. The HRTEM image, shown in Fig. 2b, confirms the nanostructured nature of the electro-catalysts, with the *d* spacing being ~0.312 nm ± 0.005 nm, that matches well with the *d*₁₁₀ spacing of pure IrO₂ which is 0.318 nm

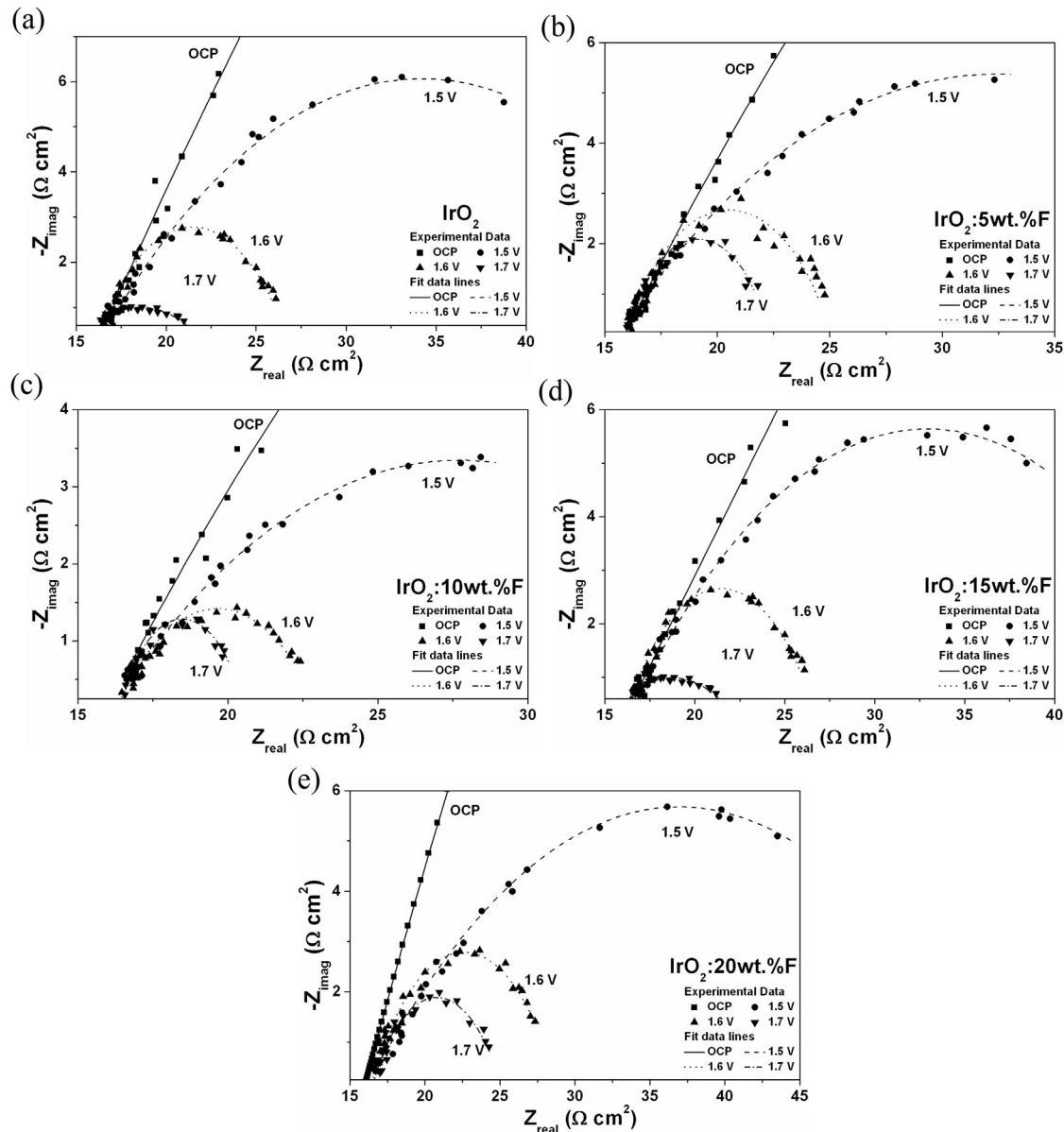


Fig. 3. EIS spectra of undoped IrO_2 (a), $\text{IrO}_2:5$ wt.% F (b), $\text{IrO}_2:10$ wt.% F (c), $\text{IrO}_2:15$ wt.% F (d) and $\text{IrO}_2:20$ wt.% F (e); obtained at OCP, 1.5 V, 1.6 V and 1.7 V (vs. NHE) in a solution of 1 N H_2SO_4 at 40 °C.

[59]. All the powders with different F content also have a particle size of ~5–10 nm which has been confirmed by high resolution TEM imaging.

3.2. Electrochemical performance and kinetics studies

The electrochemical activity of the nanostructured $\text{IrO}_2:\text{F}$ with F doping ranging from 0 to 20 wt.% has been studied as an OER catalyst for use as an anode in PEM based water electrolysis. Polarization was conducted at a scan rate of 1 mV s^{-1} in 1 N H_2SO_4 at 40 °C. The uncorrected polarization curve and the non-linear Tafel plot encounters a large amount of ohmic/solution resistance (R_s) which is determined from the electrochemical impedance spectroscopy (EIS) plot at high frequencies [27,38,40]. This helps us in preparing the linear Tafel plots and the iR corrected polarization curves. The plots after correcting for the ohmic loss help us in evaluating the inherent electro-catalytic property of the electrodes. The EIS plots of undoped IrO_2 , $\text{IrO}_2:5$ wt.% F, $\text{IrO}_2:10$ wt.% F,

$\text{IrO}_2:15$ wt.% F and $\text{IrO}_2:20$ wt.% F at open circuit potential (OCP), 1.5 V, 1.6 V and 1.7 V (vs. NHE) are plotted in Fig. 3a–e, respectively. It is observed that the R_s values obtained (Table 1) at high frequencies for all $\text{IrO}_2:\text{F}$ electrodes at various potentials is very similar

Table 1

Impedance parameters of $\text{IrO}_2:\text{F}$ obtained by fitting the experimental EIS data at open circuit potential (OCP), 1.5 V, 1.6 V and 1.7 V (vs. NHE).

	F doping (wt.%)	OCP	1.5 V	1.6 V	1.7 V
R_s ($\Omega \text{ cm}^2$)	0	15.96	15.99	16.04	16.30
	5	16.08	15.95	15.87	16.01
	10	16.07	15.87	16.17	16.39
	15	15.71	15.96	15.94	16.46
	20	15.84	15.95	16.24	16.40
R_{ct} ($\Omega \text{ cm}^2$)	0	203.4	36.42	11.53	8.13
	5	154.2	32.39	9.29	5.65
	10	126.4	23.69	6.96	3.76
	15	175.5	33.99	11.03	8.04
	20	200.8	42.00	12.75	6.98

($\sim 16.1 \pm 0.4 \Omega \text{ cm}^2$). The EIS plots show a well formed semi-circular arc at low frequencies and its diameter gives the polarization resistance (R_{ct}). Table 1 enlists the impedance parameters i.e., R_{s} and R_{ct} for all the synthesized electro-catalysts ($\text{IrO}_2:\text{F}$) at different potentials. It is observed that the R_{ct} value at all potentials decreases when F doping is increased from 0 to 10 wt.% F. R_{ct} is the resistance due to electron transfer at the electrochemical interface. A lower value of R_{ct} implies that there is less resistance offered by the electrode during the OER and as a result would lead to enhanced catalytic performance and electrochemical activity. It is also seen that the R_{ct} increases when F the doping level is elevated to 15 and 20 wt.% F (Table 1 and Fig. 3). Hence accordingly, as the R_{ct} increases, a decrease in the electrochemical activity is to be expected.

The polarization curves of the $\text{IrO}_2:\text{F}$ electro-catalysts before and after iR correction are shown in Fig. 4a and b for different F doping. Fig. 4a shows the polarization tests on nanocrystalline IrO_2 , $\text{IrO}_2:5$ wt.% F and $\text{IrO}_2:10$ wt.% F. It is clearly seen that the onset of electrolysis or the OER begins at ~ 1.43 V (vs. NHE). The current density at ~ 1.48 V after iR correction (vs. NHE), which is in the standard range of accepted voltages for determining electro-catalytic activity in PEM electrolysis conditions, is $0.0088 \pm 0.0002 \text{ A cm}^{-2}$ for undoped IrO_2 with a total loading of $\sim 0.3 \text{ mg cm}^{-2}$. At the same voltage of ~ 1.48 V and a total loading of $\sim 0.3 \text{ mg cm}^{-2}$, both $\text{IrO}_2:5$ wt.% F and $\text{IrO}_2:10$ wt.% F display a current density of $0.0133 \pm 0.0002 \text{ A cm}^{-2}$ and $0.030 \pm 0.0002 \text{ A cm}^{-2}$, respectively. Fluorine doping of 10 wt.% thus shows an appreciable increase in the current density with respect to pure IrO_2 (ca. 3.3 times) implying a substantial increase in the electrochemical activity of the catalyst. As F doping is increased to 15 and 20 wt.%, it is observed (Fig. 4b) that although the onset of the OER remains similar and is ~ 1.43 V (vs. NHE) for the catalysts, the current obtained decreases for the same loading of $\sim 0.3 \text{ mg cm}^{-2}$. The current density at ~ 1.48 V (vs. NHE) for 15 wt.% F and 20 wt.% F doped IrO_2 is $0.0112 \pm 0.0002 \text{ A cm}^{-2}$ and $0.010 \pm 0.0002 \text{ A cm}^{-2}$, respectively. These results also agree very well with the EIS plots as an increase in R_{ct} is seen after increasing F doping above 10 wt.% (Table 1 and Fig. 3). This suggests that $\text{IrO}_2:10$ wt.% F is the most optimal electro-catalyst F dopant concentration yielding very high electro-catalytic activity compared to pure IrO_2 .

Fig. 5 shows the uncorrected and iR corrected Tafel plots for $\text{IrO}_2:\text{F}$. The Tafel slope is calculated from the iR corrected Tafel plot as explained earlier (Equation (1)). An ideal Tafel slope of $\sim 62 \text{ mV dec}^{-1}$ would correspond to the well-known two electron pathway mechanism, assuming a transfer coefficient of 0.5 [39,41,60]. As seen in Fig. 5a, undoped pure IrO_2 has a Tafel slope of $\sim 93 \text{ mV dec}^{-1}$. It has been determined from Fig. 5b–e that with 5, 10, 15 and 20 wt.% F doping of IrO_2 , the Tafel slope is $\sim 77 \text{ mV dec}^{-1}$, 64 mV dec^{-1} , 85 mV dec^{-1} and 116 mV dec^{-1} , respectively. The Tafel slopes along with other RDE parameters have been reported in Table 2. The values in the Table explains the increase in electrochemical activity or current density, which is favored by a decrease in the Tafel slope with corresponding increase in F content up to 10 wt.% as demonstrated in the polarization curves (Fig. 4). These results further confirm that 10 wt.% F doped IrO_2 is the most optimized composition resulting in enhanced catalytic activity with the lowest value of the Tafel slope.

The increase in performance of IrO_2 by doping with fluorine has been theoretically dealt with by our group [32]. In the reported work, we had discussed such phenomena in the case of thin film of IrO_2 . The kinetics of oxygen evolution on IrO_2 catalysts depend on a number of sub-steps which have differing activation barriers. We believe that F doped IrO_2 configurations result in stabilization of the structures with lower activation energy barrier as evidenced by the

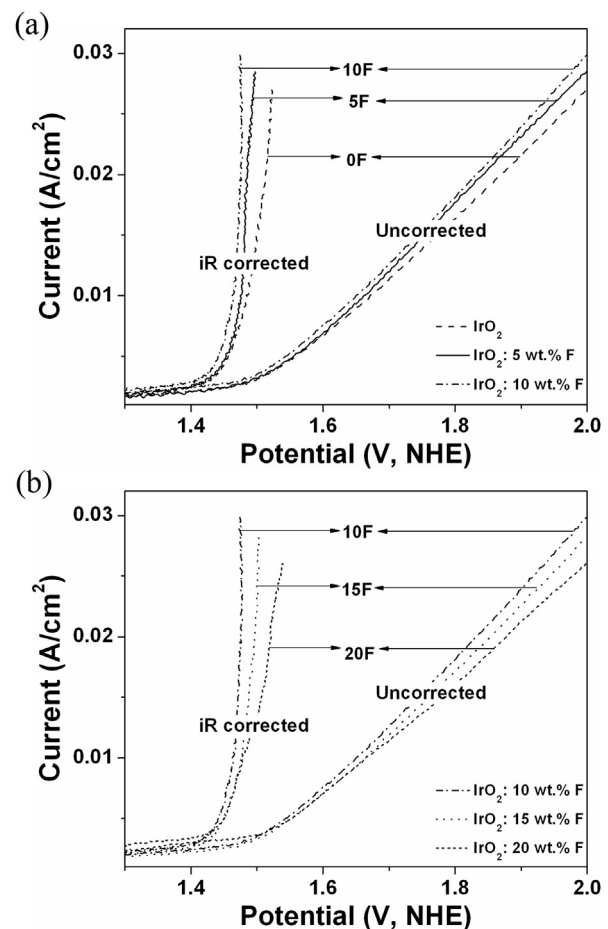


Fig. 4. Polarization testing conducted at a scan rate of 1 mV s^{-1} in $1 \text{ N H}_2\text{SO}_4$ at 40°C of undoped IrO_2 , $\text{IrO}_2:5$ wt.% F and $\text{IrO}_2:10$ wt.% F (a); and $\text{IrO}_2:10$ wt.% F, $\text{IrO}_2:15$ wt.% F and $\text{IrO}_2:20$ wt.% F (b), before and after iR correction.

R_{ct} values seen in Table 1. As shown in our prior work [32], introduction of fluorine results in a noticeable decrease of the activation barrier. With increasing F-content, there is reduction in the energy barrier and thus, there is increase in the catalytic activity of the material. However, this computational model study does not demonstrate any preconditions needed for optimal fluorine concentration beyond which there is reduction in the catalytic activity. It is possible that such a reduction of the catalytic activity with F-doping beyond 10 wt.% could be due to stabilization of the fluorine outside the IrO_2 crystal lattice and possible drop in the electronic conductivity as well as chemical stability of the system, aspects not considered in the present study but discussed in the previously published work [32]. Furthermore, our earlier published work on F doped $(\text{IrSn})\text{O}_2$ thin films which is iso-structural to IrO_2 shows that with the optimal F content, the calculated Ir d-band partial density of states (DOS) shows that the Ir d-band center matches that of IrO_2 [27], a likely indicator for the electrochemical activity for water electrolysis. It is possible that in the case of F doped IrO_2 , although not calculated in the present study, with optimal F content, in addition to the improved reaction kinetics, chemical stability and electronic conductivity, the possible shift in the Ir d-band center could also be an additional reason for the observed high electrochemical activity of the 10 wt.% F doped IrO_2 reported in this study.

It should also be noted that the ICP elemental analysis conducted on the 10 wt.% F doped IrO_2 does confirm the chemical stability since no Ir was detected in the electrolyte solution. Hence,

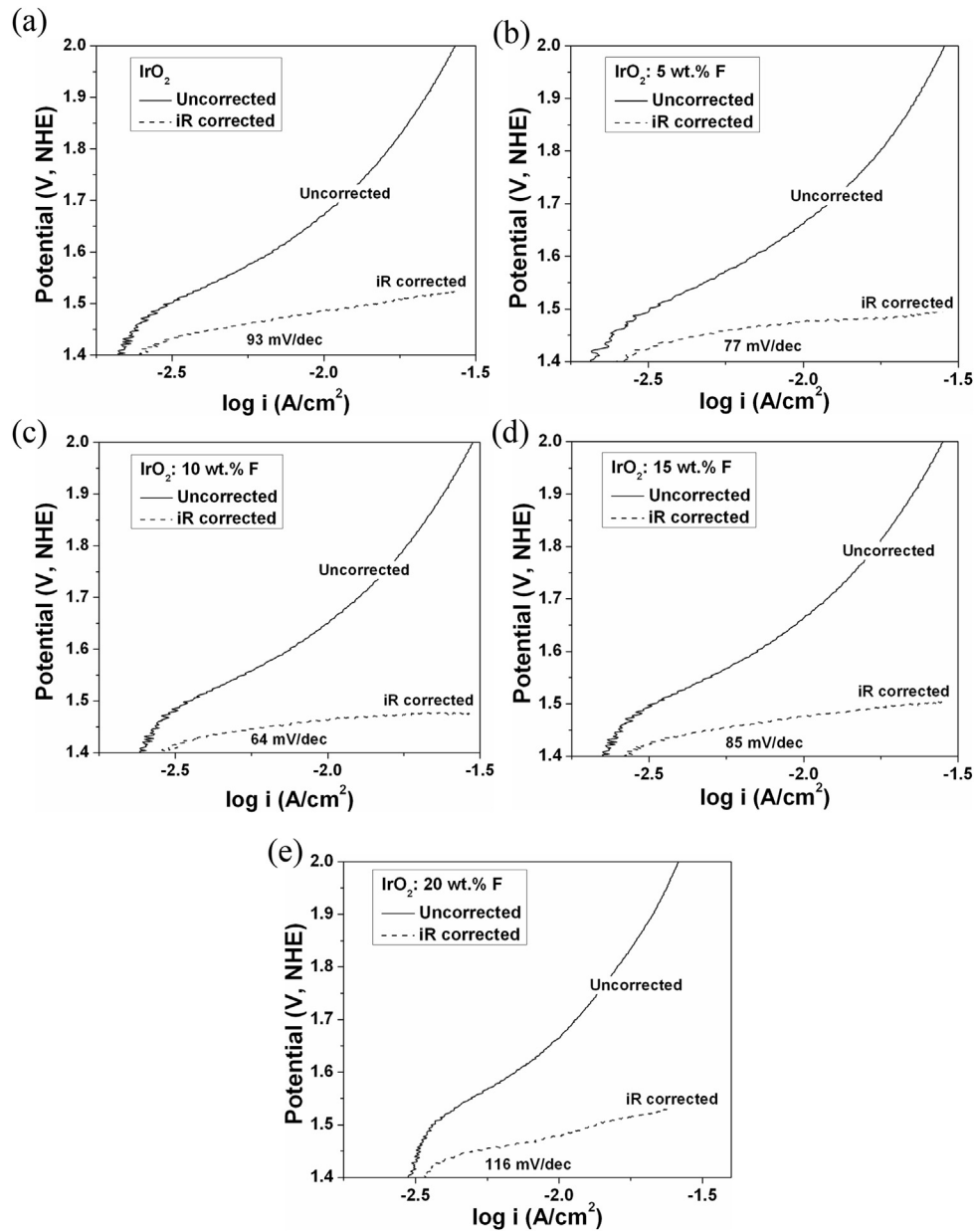


Fig. 5. The Tafel plot of undoped IrO_2 (a), $\text{IrO}_2:5$ wt.% F (b), $\text{IrO}_2:10$ wt.% F (c), $\text{IrO}_2:15$ wt.% F (d) and $\text{IrO}_2:20$ wt.% F (e); before and after iR correction.

the electronic conductivity and chemical stability of the 10 wt.% F doped IrO_2 combined with possible shift in Ir-d band center points to the observed improved electrochemical performance for this composition. Based on the above, the exact reasons for the drop in electrochemical performance with doping of IrO_2 beyond 10 wt.% F are not clear. Nevertheless, such trends were also observed in the case of thin-film F-doped IrO_2 films previously reported as well [31]. Changes in electronic conductivity with change in fluorine content have previously been reported for SnO_2 thin film materials [61]. Additionally, the presence of fluorine possibly introduces oxygen vacancies and other point defects resulting in a drop in conductivity beyond a particular concentration.

Multiple small potential step voltammetry was performed for the rotating disk electrode studies in order to study the fundamental reaction kinetics and also calculate the apparent activation energy of the OER process. The catalyst ink coated Ti disk insert was rotated at various speeds ranging from 500 rpm to 2000 rpm.

Fig. 6a–e shows the Koutecky–Levich plot *i*^{−1} vs. $\omega^{-1/2}$ for $\text{IrO}_2:x$ wt.% F; where $x = 0, 5, 10, 15$ and 20 , respectively. The current values at different rotation speeds have been plotted at three potentials of 1.55 V, 1.65 V and 1.75 V (vs. NHE) without iR correction. It should be noted that the potentials were not iR corrected since the tests have been conducted *in-situ* (*via* multiple small potential step voltammetry) from which the RDE results are reported directly. This dynamic testing process does not allow accounting for the iR drop from the solution resistance. These RDE plots at different potentials give parallel straight lines (**Fig. 6**) of similar nature; and the current increases with increase in voltage as expected, causing a decrease in the value of i^{-1} . At any given potential and rotation speed, it is observed that the current density is increased significantly when the F doping is increased up to 10 wt.% and then decreases with 15 and 20 wt.% F doping. This trend is thus consistent with the results obtained from the polarization curves (**Fig. 4**). From the slope of the graphs, the number of electrons

Table 2

The Tafel slope, number of electrons transferred in the OER and the kinetic rate constants determined from the Koutecky–Levich plots for $\text{IrO}_2\text{-F}$.

F doping (wt.%)	Tafel slope (mV dec ⁻¹)	n	k (cm s ⁻¹)		
			1.55 V	1.65 V	1.75 V
0	93	1.78	0.0618	0.0708	0.0826
5	77	1.86	0.0660	0.0763	0.0853
10	64	1.92	0.0656	0.0717	0.0823
15	85	1.82	0.0652	0.0743	0.0874
20	116	1.61	0.0679	0.0810	0.1010

transferred (*n*) is determined following Equations (2) and (4). The average value of '*n*' determined at the three voltages for all $\text{IrO}_2\text{-F}$ electro-catalysts along with the Tafel slope and kinetic rate constant (*k*) has been tabulated in Table 2. The kinetic rate constant (calculated using Equation (3)) of an electrochemical reaction not

only varies with the applied potential, but is also dependent on many other factors viz., temperature, electrode surface structure, composition of the catalyst, surface adsorption and reaction intermediates [45,51,62,63]. The RDE tests and the Koutecky–Levich plot confirm the two electron pathway mechanism for the OER in PEM electrolysis for all our explored catalyst compositions. The '*n*' value is closest to 2 for $\text{IrO}_2\text{-10 wt.% F}$ doped electro-catalyst (Table 2 and Fig. 6c) corroborating the fact that it is the best composition amongst all the other F doped and undoped IrO_2 electro-catalyst. Increased F doping (above 10 wt.% F) leads to slight decrease in the '*n*' value which is the number of electrons transferred during the OER. This is because the polarization resistance increases as observed in the impedance plots (Fig. 3 and Table 1), impeding the electron transfer process in the electrochemical interface. This in turn also yields lesser values of current density for the catalysts with higher F doping amounts as seen in the polarization curves (Fig. 4b). This further elucidates the high

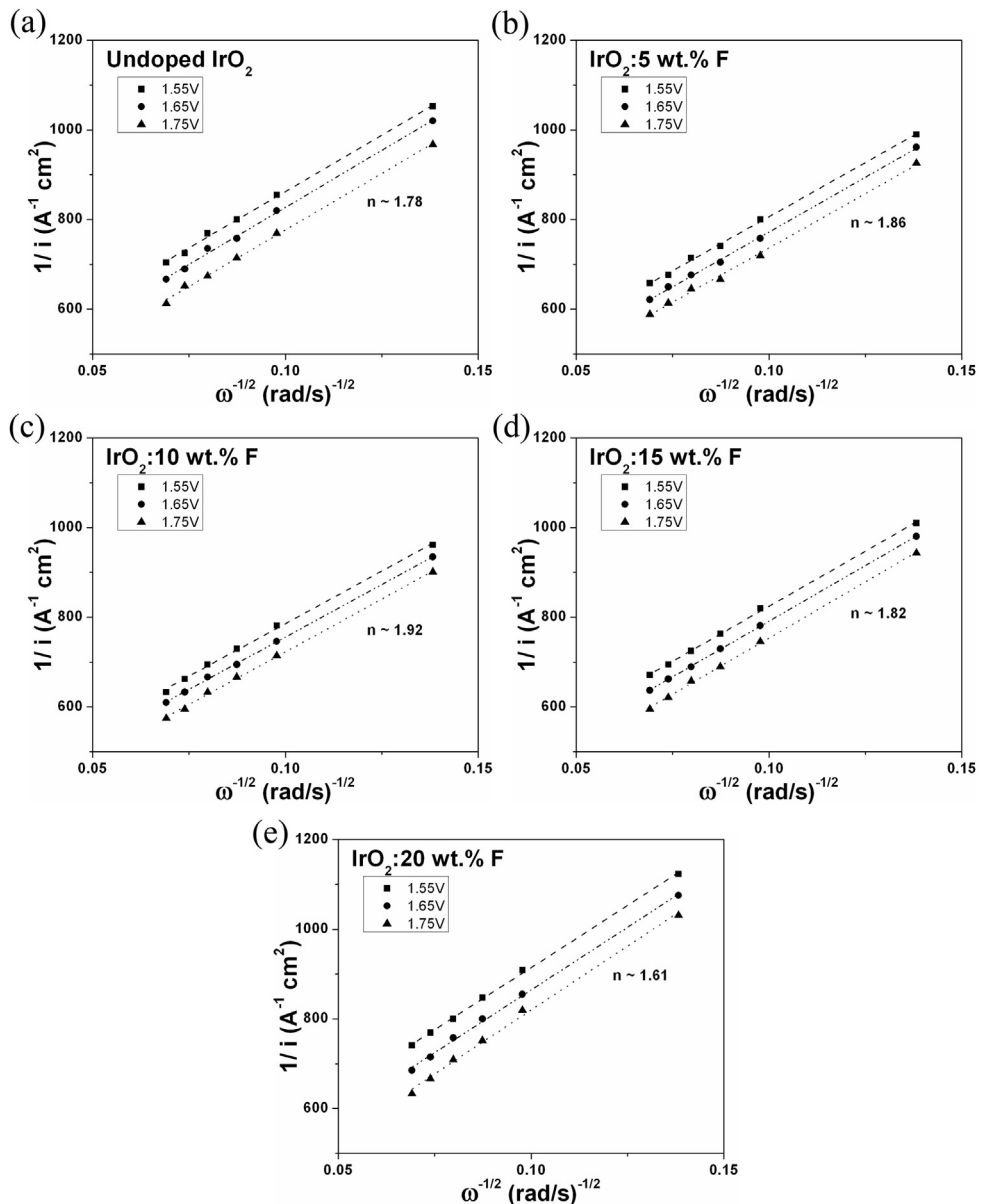


Fig. 6. Koutecky–Levich plots in PEM based water electrolysis at 1.55 V, 1.65 V and 1.75 V (vs. NHE) in 1 N H_2SO_4 at 25 °C for undoped IrO_2 (a), $\text{IrO}_2\text{-5 wt.% F}$ (b), $\text{IrO}_2\text{-10 wt.% F}$ (c), $\text{IrO}_2\text{-15 wt.% F}$ (d) and $\text{IrO}_2\text{-20 wt.% F}$ (e).

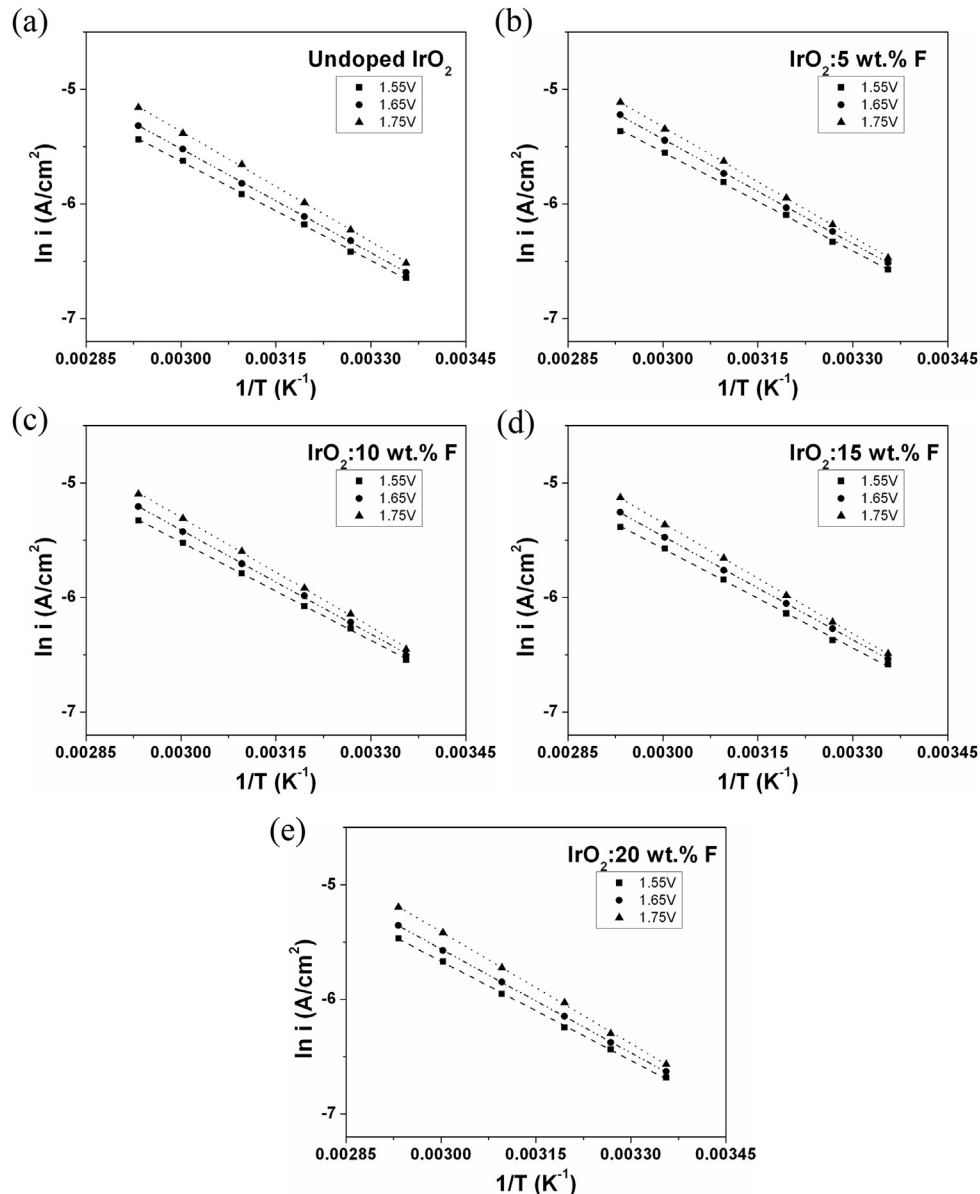
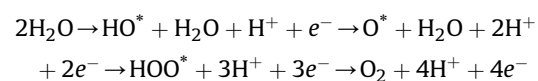


Fig. 7. Arrhenius plots for undoped IrO_2 (a), $\text{IrO}_2:5$ wt.% F (b), $\text{IrO}_2:10$ wt.% F (c), $\text{IrO}_2:15$ wt.% F (d) and $\text{IrO}_2:20$ wt.% F (e) at 1.55 V, 1.65 V and 1.75 V (vs. NHE) over a temperature range of 25 °C–70 °C in 1 N H_2SO_4 .

electrochemical activity and the close to ideal Tafel slope of the 10 wt.% F doped IrO_2 , thus indicating it to be a preferred OER electro-catalyst composition for PEM electrolyzer cells.

The influence of temperature on the OER was studied in order to calculate the apparent activation energy from the Arrhenius relationship as explained before (Equation (5)). The Arrhenius plots *i.e.*, $\ln i$ vs. T^{-1} for $\text{IrO}_2:x$ wt.% F where $x = 0, 5, 10, 15$ and 20 are shown in Fig. 7a–e, respectively. The temperature was varied between 25 and 70 °C and data points in these graphs have been plotted at three different potentials of 1.55 V, 1.65 V and 1.75 V (vs. NHE) as used before in the RDE tests. The slopes of these lines was averaged in order to calculate the E_a which is obtained to be $-25.2 \pm 1.5 \text{ kJ mol}^{-1}$ for all the IrO_2 :F electro-catalysts. This E_a value is lower and in the range and order of values reported for OER by other researchers [50,52,64–67]. The similar E_a value for all the electrodes suggests that the OER on all electrodes proceeds *via* an identical reaction mechanism [52,68]. The reaction mechanism has

been previously reported by Nørskov et al. and in our earlier publication [32,41,69]. The four step reaction mechanism occurring during PEM based water electrolysis is well known and can be indicated as follows:



Here, the * represents an active site on the metal oxide surface and the third step is the rate determining/limiting step in the electrolysis reaction [32,41,69]. Although there is no difference in the activation barrier owing to similar E_a values for all the synthesized powder catalysts, the inherent kinetics are most optimal for the $\text{IrO}_2:10$ wt.% F electro-catalyst possibly due to difference in the activity and number of catalytically active sites [68]. This is not only confirmed by the data reported in the polarization curves

(Fig. 4), but is also evident from the different 'n' values obtained from the Koutecky–Levich plots (Fig. 6). This is because of the difference in the anodic polarization and charge transfer properties as observed in the impedance and Tafel plots (Figs. 3 and 5).

The robustness and chemical stability of the synthesized electro-catalysts have been studied by chronoamperometry (CA) testing. Fig. 8 shows the CA curves for the IrO_2 :F catalysts conducted at a constant voltage of ~ 1.65 V (vs. NHE) without iR correction for 12 h. The IrO_2 :10 wt.% F electrode shows higher current than the other electrodes since it inherently has a higher catalytic activity as observed in the polarization curves (Fig. 4). A steady decay of current may arise due to the dissolution of the catalyst material along the edges of the support [16,17,60], or due to continuous exhaustion of the electrolyte/fuel (H_2SO_4) owing to the high electrochemical activity of the electro-catalysts [31,34,70]. It is evident in Fig. 8 by the slope of the different curves that the higher fluorine doped catalysts *i.e.*, IrO_2 doped with 15 and 20 wt.% F degrade slightly faster than the undoped, 5 and 10 wt.% F doped IrO_2 . The powder electro-catalyst material exhibiting superior electrochemical activity reported herein (IrO_2 :10 wt.% F), also shows excellent durability and current retention. On an overall basis, the CA response shows an acceptable stability with respect to the drop in current observed and reported widely by researchers in other publications [27,70,71]. Inductively coupled plasma optical emission spectroscopy (ICP-OES) studies were conducted on the electrolyte media after the conclusion of the CA test (*i.e.*, after 12 h). It should be noted that no Ir was found to have leached out from any of the F doped or undoped IrO_2 catalysts, confirming that the drop in current is primarily due to the exhaustion of the fuel owing to the high catalytic activity of the nanostructured powder electro-catalysts. These stability results further complement and strengthen our earlier claims and findings; suggesting that IrO_2 :10 wt.% F electro-catalyst is an optimized composition for use as an OER anode catalyst in PEM based water electrolysis.

Finally, the optimally performing electro-catalyst composition IrO_2 :10 wt.% F in half cell tests was further tested at Proton OnSite in a single full cell set-up for PEM based water electrolysis. These results were compared with undoped pure IrO_2 which was also tested under identical conditions. The polarization curve, shown in Fig. 9, was obtained by ramping up and down the current at 1 min intervals until the forward and reverse scans overlaid each other. It is seen that the 10 wt.% F doped IrO_2 electro-catalyst exhibits much superior electro-catalytic activity compared to the undoped counterpart. The current density at ~ 2 V, a standard

assessment voltage considered for single full PEM electrolyzer tests, is $\sim 1.1 \text{ A cm}^{-2}$ and $\sim 0.5 \text{ A cm}^{-2}$ for IrO_2 :10 wt.% F and IrO_2 , respectively. This implies an approximately 2.2 fold increase in the current for the F doped electro-catalyst with respect to pure IrO_2 . This is in good agreement with the polarization curves (Fig. 4a) correspondingly reflecting the increase in current observed. The polarization curves in the half cell and full cell set-up, along with the electrochemical impedance spectra, Tafel plots and the RDE graphs reported serve to confirm that the 10 wt.% F doping enhances the electrochemical activity of IrO_2 to a very large extent demonstrating its potential as a viable OER catalyst for PEM based water electrolysis. Trends shown are similar in the case of the half cell and full-cell polarization curves. This is to be expected since the 10% F– IrO_2 material has more facile kinetics which is reflected in the R_{ct} values seen in Table 1 and the Tafel slope seen in Table 2. The improvement in performance is more significant in the single-cell full-cell as compared to the half-cell possibly because the kinetics and electronic conductivity play a bigger role in a full-cell configuration as compared to the half-cell.

4. Conclusion

In the present experimental study, nanostructured F doped IrO_2 was synthesized by a wet chemical approach and studied as an anode catalyst for the OER in PEM based water electrolysis. A modified Adams fusion method using NaNO_3 , fluoride precursors, and heat treatment of the salt mixture to 500 °C was employed to obtain high specific surface area IrO_2 and F doped IrO_2 electro-catalysts. The XRD pattern confirmed formation of a complete solid solution and the particle size was ~ 5 – 10 nm confirmed by HRTEM as well. The superior electro-catalytic OER activity of the nanometer sized F doped powders was conducted in a 1 N H_2SO_4 electrolyte/fuel at 40 °C. The electrochemical performance of 10 wt.% F doped IrO_2 was much better than undoped pure IrO_2 in both half cell and full single cell test evaluations, which was further reinforced by the Tafel plots and the EIS spectra. Detailed kinetic studies involving RDE were also conducted on all the catalysts which not only yielded the number of electrons transferred in the reaction, but also strengthened our claim that IrO_2 :10 wt.% F is the most optimally performing electro-catalyst composition explored in this study. The long term structural and chemical stability of the IrO_2 :F catalysts was comparable to pure IrO_2 thus making them a viable candidate for use as an OER catalyst. The excellent catalytic

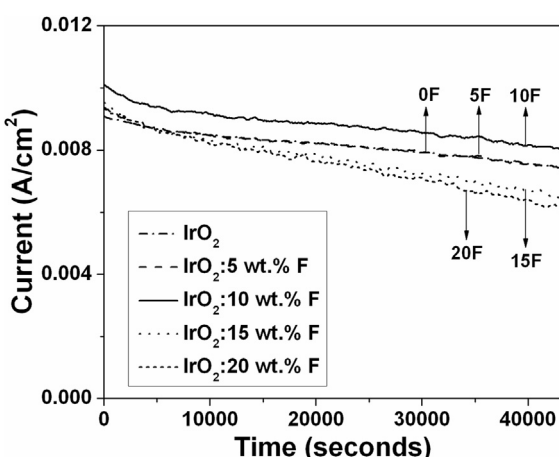


Fig. 8. The variation of current vs. time for the IrO_2 :F electrodes in 1 N H_2SO_4 under a constant potential of ~ 1.65 V at 40 °C.

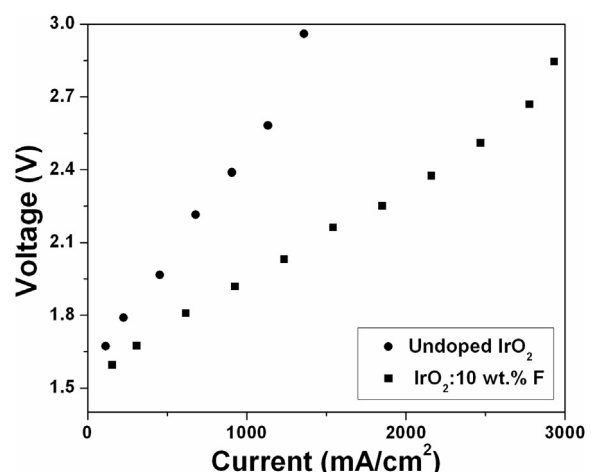


Fig. 9. Polarization curve obtained in a single full cell test for undoped IrO_2 and IrO_2 :10 wt.% F at 50 °C.

activity and durability of $\text{IrO}_2:10$ wt.% F however makes it a preferred and an ideal electro-catalyst for oxygen evolution in PEM electrolyzer cells.

Acknowledgments

Research supported by the U.S. Department of Energy, Office of Basic Energy Sciences, Division of Materials Sciences and Engineering under Award DE-SC0001531 and the National Science Foundation fund Award CBET Grant # 0933141. P.N.K. acknowledges the Edward R. Weidlein Chair Professorship Funds and the Center for Complex Engineered Multifunctional Materials (CCEMM) for procuring the electrochemical equipment and facilities used in this research work. The authors also acknowledge Proton OnSite and Dr. Kathy Ayers and the Proton Onsite team for performing the full single cell PEM electrolyzer tests.

References

- [1] C.J. Winter, Int. J. Hydrogen Energy 34 (2009) S1–S52.
- [2] G.F. Naterer, M. Fowler, J. Cotton, K. Gabriel, Int. J. Hydrogen Energy 33 (2008) 6849–6857.
- [3] F. Barbir, Chapter Twelve – Future of Fuel Cells and Hydrogen, in: PEM Fuel Cells, second ed., Academic Press, Boston, 2013, pp. 469–508.
- [4] G.W. Crabtree, M.S. Dresselhaus, M.V. Buchanan, Phys. Today 57 (2004) 39–44.
- [5] F. Barbir, Sol. Energy 78 (2005) 661–669.
- [6] P. Millet, N. Mbemba, S.A. Grigoriev, V.N. Fateev, A. Aukuloo, C. Etievant, Int. J. Hydrogen Energy 36 (2011) 4134–4142.
- [7] K. Zeng, D.K. Zhang, Prog. Energy Combust. Sci. 36 (2010) 307–326.
- [8] Y.H.P. Zhang, W.-D. Huang, Trends Biotechnol. 30 (2012) 301–306.
- [9] K. Hedegaard, P. Meibom, Renewable Energy 37 (2012) 318–324.
- [10] M. Carmo, D.L. Fritz, J. Mergel, D. Stolten, Int. J. Hydrogen Energy 38 (2013) 4901–4934.
- [11] Q. He, T. Mugadza, X. Kang, X. Zhu, S. Chen, J. Kerr, T. Nyokong, J. Power Sources 216 (2012) 67–75.
- [12] R.E. Clarke, S. Giddey, S.P.S. Badwal, Int. J. Hydrogen Energy 35 (2010) 928–935.
- [13] J.I. Levene, M.K. Mann, R.M. Margolis, A. Milbrandt, Sol. Energy 81 (2007) 773–780.
- [14] S. Pedrazzi, G. Zini, P. Tartarini, Renewable Energy 46 (2012) 14–22.
- [15] M.W. Kanan, D.G. Nocera, Science 321 (2008) 1072–1075.
- [16] K. Kadakia, M.K. Datta, O.I. Velikokhatnyi, P. Jampani, S.K. Park, S.J. Chung, P.N. Kumta, J. Power Sources 245 (2014) 362–370.
- [17] K. Kadakia, M.K. Datta, O.I. Velikokhatnyi, P. Jampani, S.K. Park, P. Saha, J.A. Poston, A. Manivannan, P.N. Kumta, Int. J. Hydrogen Energy 37 (2012) 3001–3013.
- [18] A. Marshall, B. Borresen, G. Hagen, M. Tsyplkin, R. Tunold, Electrochim. Acta 51 (2006) 3161–3167.
- [19] A.T. Marshall, S. Sunde, M. Tsyplkin, R. Tunold, Int. J. Hydrogen Energy 32 (2007) 2320–2324.
- [20] A.V. Nikiforov, A.L.T. Garcia, I.M. Petrushina, E. Christensen, N.J. Bjerrum, Int. J. Hydrogen Energy 36 (2011) 5797–5805.
- [21] K.M. Papazisi, A. Siokou, S. Balomenou, D. Tsiplikides, Int. J. Hydrogen Energy 37 (2012) 16642–16648.
- [22] F.M. Sapountzi, S.C. Divane, E.I. Papaioannou, S. Souentie, C.G. Vayenas, J. Electroanal. Chem. 662 (2011) 116–122.
- [23] S.D. Song, H.M. Zhang, X.P. Ma, Z.G. Shao, R.T. Baker, B.L. Yi, Int. J. Hydrogen Energy 33 (2008) 4955–4961.
- [24] Y. Takaue, N. Yoshinaga, W. Sugimoto, Electrochim. Commun. 10 (2008) 668–672.
- [25] Q. Wang, F. Wu, N. Wang, L. Wang, X. Zhang, Electrochim. Acta 74 (2012) 227–234.
- [26] X. Wu, K. Scott, Int. J. Hydrogen Energy 36 (2011) 5806–5810.
- [27] M.K. Datta, K. Kadakia, O.I. Velikokhatnyi, P.H. Jampani, S.J. Chung, J.A. Poston, A. Manivannan, P.N. Kumta, J. Mater. Chem. A 1 (2013) 4026–4037.
- [28] C.P. Depauli, S. Trasatti, J. Electroanal. Chem. 396 (1995) 161–168.
- [29] M. Morimitsu, R. Otogawa, M. Matsunaga, Electrochim. Acta 46 (2000) 401–406.
- [30] S. Ardizzone, C.L. Bianchi, G. Cappelletti, M. Ionita, A. Minguzzi, S. Rondinini, A. Vertova, J. Electroanal. Chem. 589 (2006) 160–166.
- [31] K. Kadakia, M.K. Datta, P.H. Jampani, S.K. Park, P.N. Kumta, J. Power Sources 222 (2013) 313–317.
- [32] O.I. Velikokhatnyi, K. Kadakia, M.K. Datta, P.N. Kumta, J. Phys. Chem. C 117 (2013) 20542–20547.
- [33] O.I. Velikokhatnyi, P.N. Kumta, Phys. B Condens. Matter 406 (2011) 471–477.
- [34] K. Kadakia, M.K. Datta, O.I. Velikokhatnyi, P.H. Jampani, P.N. Kumta, Int. J. Hydrogen Energy 39 (2014) 664–674.
- [35] R. Adams, R.L. Shriner, J. Am. Chem. Soc. 45 (1923) 2171–2179.
- [36] J. Cheng, H. Zhang, G. Chen, Y. Zhang, Electrochim. Acta 54 (2009) 6250–6256.
- [37] E. Mayousse, F. Maillard, F. Fouad-Onana, O. Sicardy, N. Guillet, Int. J. Hydrogen Energy 36 (2011) 10474–10481.
- [38] A. Minguzzi, F.-R. Fan, A. Vertova, S. Rondinini, A.J. Bard, Chem. Sci. 3 (2012) 217–229.
- [39] E. Rasten, G. Hagen, R. Tunold, Electrochim. Acta 48 (2003) 3945–3952.
- [40] N. Krstajic, S. Trasatti, J. Appl. Electrochem. 28 (1998) 1291–1297.
- [41] J. Rossmeisl, Z.W. Qu, H. Zhu, G.J. Kroes, J.K. Norskov, J. Electroanal. Chem. 607 (2007) 83–89.
- [42] R. Jiang, D. Chu, Electrochim. Acta 45 (2000) 4025–4030.
- [43] K.J.J. Mayrhofer, D. Strmcnik, B.B. Blizanac, V. Stamenkovic, M. Arenz, N. Markovic, Electrochim. Acta 53 (2008) 3181–3188.
- [44] T.J. Schmidt, H.A. Gasteiger, G.D. Stäb, P.M. Urban, D.M. Kolb, R.J. Behm, J. Electrochim. Soc. 145 (1998) 2354–2358.
- [45] E. Lust, E. Härk, J. Nerut, K. Vaarmets, Electrochim. Acta 101 (2013) 130–141.
- [46] R.N. Itoe, G.D. Wesson, E.E. Kalu, J. Electrochim. Soc. 147 (2000) 2445–2450.
- [47] S. Gottesfeld, I.D. Raistrick, S. Srinivasan, J. Electrochim. Soc. 134 (1987) 1455–1462.
- [48] K.E. Gubbins, R.D. Walker, J. Electrochim. Soc. 112 (1965) 469–471.
- [49] M.M. Hefny, S. Abdel-Wanees, Electrochim. Acta 41 (1996) 1419–1422.
- [50] E.M. García, H.A. Taróco, T. Matencio, R.Z. Domingues, J.A.F. dos Santos, Int. J. Hydrogen Energy 37 (2012) 6400–6406.
- [51] J.L. Cohen, D.J. Volpe, H.D. Abruna, Phys. Chem. Chem. Phys. 9 (2007) 49–77.
- [52] L.M. Da Silva, D.V. Franco, L.A. De Faria, J.F.C. Boodts, Electrochim. Acta 49 (2004) 3977–3988.
- [53] E.J.W. Whittaker, R. Muntus, Geochim. Cosmochim. Acta 34 (1970) 945–956.
- [54] T.H. de Keijser, J.I. Langford, E.J. Mittemeijer, A.B.P. Vogels, J. Appl. Crystallogr. 15 (1982) 308–314.
- [55] N. Todorova, T. Giannakopoulou, G. Romanos, T. Vaimakis, J. Yu, C. Trapalis, Int. J. Photoenergy 2008 (2008).
- [56] C. Papadopoulou, A. Lycourghiotis, P. Grange, B. Delmon, Appl. Catal. 38 (1988) 255–271.
- [57] A.K. Ghosh, R.A. Kydd, Catal. Rev. 27 (1985) 539–589.
- [58] J. Ramirez, R. Cuevas, A.L. Agudo, S. Mendioroz, J.L.G. Fierro, Appl. Catal. 57 (1990) 223–240.
- [59] A.A. Bolzan, C. Fong, B.J. Kennedy, C.J. Howard, Acta Crystallogr. Sect. B Struct. Sci. 53 (1997) 373–380.
- [60] J.M. Hu, H.M. Meng, J.Q. Zhang, C.N. Cao, Corros. Sci. 44 (2002) 1655–1668.
- [61] A.E. Rakhshani, Y. Makdisi, H.A. Ramazaniyan, J. Appl. Phys. 83 (1998) 1049–1057.
- [62] A. Damjanovic, J. Electroanal. Chem. 355 (1993) 57–77.
- [63] R. Jiang, F.C. Anson, J. Electroanal. Chem. Interfacial Electrochem. 305 (1991) 171–184.
- [64] L.M. Da Silva, L.A. De Faria, J.F.C. Boodts, Electrochim. Acta 48 (2003) 699–709.
- [65] A. Mills, H.L. Davies, Electrochim. Acta 37 (1992) 1217–1225.
- [66] S. Siracusano, V. Baglio, A. Di Blasi, N. Briguglio, A. Stassi, R. Ornelas, E. Trifoni, V. Antonucci, A.S. Aricò, Int. J. Hydrogen Energy 35 (2010) 5558–5568.
- [67] S. Ardizzone, M. Falcicola, S. Trasatti, J. Electrochim. Soc. 136 (1989) 1545–1550.
- [68] H. Tamura, C. Iwakura, Int. J. Hydrogen Energy 7 (1982) 857–865.
- [69] J. Rossmeisl, A. Logadottir, J.K. Norskov, Chem. Phys. 319 (2005) 178–184.
- [70] J.C. Cruz, S. Rivas, D. Beltran, Y. Meas, R. Ornelas, G. Osorio-Monreal, L. Ortiz-Frade, J. Ledesma-García, L.G. Arriaga, Int. J. Hydrogen Energy 37 (2012) 13522–13528.
- [71] V. Natarajan, S. Basu, K. Scott, Int. J. Hydrogen Energy 38 (2013) 16623–16630.